Journal of Environmental Radioactivity 219 (2020) 106283

Contents lists available at ScienceDirect

Journal of Environmental Radioactivity

journal homepage: www.elsevier.com/locate/jenvrad

Ambient radioactivity and atmospheric electric field: A joint study in an urban environment

Susana Barbosa *

INESC TEC - INESC Technology and Science, Porto, Portugal

ARTICLE INFO

Keywords:
Radioactivity
Electric field
Radon
Atmosphere
Ionisation

ABSTRACT

Ambient radioactivity and atmospheric electricity are inextricably linked phenomena. In order to assess the role of ambient radioactivity in the local variability of the atmospheric electric field at an urban site, simultaneous measurements of radon concentration, gamma radiation, and atmospheric electric field are carried out in the city of Porto, Portugal. Both radon and gamma radiation display an average daily cycle peaking before sunrise, but with considerable variability from day to day, particularly in amplitude. The atmospheric electric field displays a daily cycle with a minimum at dawn and maximum in the early afternoon, as well as a secondary peak in the early morning. The temporal variation of the daily patterns is analysed by means of an empirical orthogonal function analysis, and related to local meteorological parameters. The variability of the local atmospheric electric field is mainly determined by aerosol transport and accumulation close to the surface associated with local meteorological conditions and atmospheric stability rather than by conductivity variations associated with ambient radioactivity.

1. Introduction

Ambient radioactivity and atmospheric electricity are inextricably linked phenomena. The connection between the electrical properties of the lower atmosphere and radioactivity at the earth's surface was established in the early 20th century, when Elster and Geitel found that radioactivity was responsible for the ionisation of the air (Fricke and Schlegel, 2017). Later evidence of increased atmospheric ionisation with altitude lead to the discovery of cosmic radiation (Hess, 1912). Ionising radiation associated with both cosmic radiation and radioactive decay produces ions via the ionisation of air molecules (nitrogen, oxygen, and trace species) which move in the Earth's electric field driving a fair-weather electric current flowing through the atmosphere to the Earth (Rycroft et al., 2000; Harrison and Carslaw, 2003).

The concept of a global atmospheric electric circuit sustained by an air–Earth conduction current driven by thunderstorms and rain clouds was put forward by Wilson (1921, 1924) to explain the diverse measurements in the 18th and 19th centuries showing the existence of a permanent electric field in the atmosphere, even in the absence of thunderstorms and lightning (Aplin et al., 2008). The global nature of the electric circuit was demonstrated thanks to electric field measurements performed in oceanic air by the geophysical survey vessel Carnegie from 1909 to 1929 (Harrison, 2013). The detailed electric field measurements allowed to identify a diurnal pattern following Universal Time (with maximum around 19UT and minimum around 03UT) independent of the location, known now as the Carnegie curve, and associated with global lightning activity (Kartalev et al., 2006; Anisimov and Mareev, 2008; Williams, 2009).

The atmospheric electric field at a given location is the result of local factors superimposed on the global electric circuit fair weather component. Local contributions are driven by processes able to locally alter the space charge density or the ion mobility (Harrison and Carslaw, 2003). Thus meteorological conditions significantly impact the local atmospheric electric field (Bennett and Harrison, 2007; Yaniv et al., 2019), as well as fog (Piper and Bennett, 2012), clouds (Nicoll and Harrison, 2016; Harrison et al., 2017), aerosols (Israelsson and Lelwala, 1999; Harrison and Aplin, 2003; Aplin, 2012) and dust (Silva et al., 2016; Yair et al., 2016; Harrison et al., 2018). Aerosols reduce the atmospheric conductivity via the attachment of ions to aerosols and reduction of the mobility of small ions (Nagaraja et al., 2006; Harrison and Tammet, 2008; Wright et al., 2014), enhancing the electric field. Increased unattached ion concentration and/or ion mobility is expected to decrease the electric field by increasing conductivity.

Ion production in the atmosphere is mainly driven by ionising radiation resulting from radioactive decay (Zhang et al., 2011; Chen et al., 2016a) and from cosmic radiation, particularly muons (Goldhagen, 2000; Wissmann et al., 2005). In the lower atmosphere Radon (Rn-222) and its progeny are the major source of ionising radiation.

* Correspondence to: INESC TEC, Campus da FEUP, R Dr Roberto Frias, 4200-465 Porto, Portugal.
E-mail address: susana.a.barbosa@inesctec.pt.

https://doi.org/10.1016/j.jenvrad.2020.106283
Received 18 August 2019; Received in revised form 28 April 2020; Accepted 28 April 2020
Available online 30 April 2020

Unlike other radionuclides which are solid and thus remain bound to the earth's surface, radon is a radioactive gas and as such it is highly mobile and can be released from the earth surface into the atmosphere. Emission of radon gas depends on local features, such as the radium content of the surface or the porosity and permeability of the radium-containing medium, and also on the multiple processes influencing the diffusive and advective movement of radon in the subsurface (Barbosa et al., 2015). Thus the emission of radon into the lower atmosphere is very dependent on highly variable meteorological conditions including temperature, pressure, and soil moisture (Lebedyte et al., 2003; Barbosa et al., 2010; Zafrir et al., 2013). Radon exhaled from the surface can rapidly disperse up to several km from the surface depending on a complex interplay of local atmospheric conditions, in particular the height of the mixing layer (Sesana et al., 2006; Chambers et al., 2011; Pal et al., 2015; Chen et al., 2016b; Anisimov et al., 2018). Variations in radon concentration through the lower troposphere are mainly related to vertical mixing processes (Williams et al., 2011; Chambers et al., 2019). Local transport of airborne radon, strongly dependent on wind conditions, is a further contribution to local sources of ionising radiation (Arrillaga et al., 2018; Melintescu et al., 2018).

In addition to the ionising radiation (alpha and beta particles as well as gamma rays) resulting from the radioactive decay of airborne radon and its progeny, a further driver of ion production in the atmosphere is the terrestrial gamma radiation resulting from the radioactive decay of radon and of natural radionuclides (mainly K-40 and radionuclides from the U and Th decay series) in the upper 50 cm of the earth's surface (Gasser et al., 2014). Although the concentration of natural radionuclides in the ground is stable, the corresponding gamma-ray flux above ground is highly variable as the gamma-ray attenuation is very dependent on the soil water content (Barbosa et al., 2018). A further source of gamma radiation in the lower atmosphere and at the earth's surface are gamma-emitting aerosols brought down from the troposphere by precipitation as a result of both in-cloud scavenging and below-cloud washout processes (Paatero and Hatakka, 1999; Melintescu et al., 2018). Most airborne radon progeny readily attach to the surface of aerosol particles (Porstendörfer et al., 2000), and thus their behaviour is strongly determined by the size and density distribution of aerosol particles (Grundel and Porstendorfer, 2004). Therefore gamma radiation near the earth's surface displays considerable temporal variability resulting from the complex interplay of precipitation, soil moisture, radon exhalation, and gamma emission processes (Barbosa et al., 2017; Bossew et al., 2017; Melintescu et al., 2018).

Improving the current understanding of the atmospheric electric field, and its connection to atmospheric ionisation and ambient radioactivity, is relevant for diverse areas and applications. The electric field is very sensitive to the presence of aerosols, and thus it is considered a useful parameter for assessing aerosol pollution in urban areas (Wang et al., 2018) The atmospheric electric field is also of interest for space weather and near space studies, as it is influenced by external sources of ionisation such as galactic cosmic rays and solar energetic particles, which are modulated by the Earth's magnetosphere and solar variability (Rycroft and Harrison, 2012). From a climate perspective the expected stronger convection in a warmer planet, and associated changes in thunderstorms, leads to an increase of the ionospheric potential (V_i) and consequent changes in Earth's global electric circuit (Price, 1993; Williams, 2009). Furthermore the charge of cloud droplets and aerosol particles is thought to influence several cloud microphysical processes, with implications to Earth's radiative balance and thus climate (Rycroft et al., 2000).

Despite the strong link between the variability of the atmospheric electric field and environmental radioactivity driven by atmospheric ionisation, as summarised in Fig. 1, few studies exist based on actual measurements of the atmospheric electric field and simultaneous measurements of environmental radioactivity (Latha, 2007; Lopes et al., 2015; Anisimov et al., 2018). The present study addresses this need by simultaneous monitoring of atmospheric radon concentration, gamma radiation, and atmospheric electric field at an urban site. In air with considerable aerosol loading, as is very often the case in urban areas, the atmospheric electric field is highly variable due to the dominant contribution of small-scale processes altering the local space charge and/or ion mobility. This study aims to provide an observation-based description of local variability by means of a detailed statistical analysis of rare simultaneous measurements of electric field and ambient radioactivity.

2. Materials and methods

2.1. Measurement site

Measurements were performed on the rooftop of the INESC TEC building located in the Asprela University Campus in the north of the city of Porto, Portugal, close to the coast, ~ 8 km (Fig. 2). The building is 20 m tall, and the instruments are mounted 2.5 m above the rooftop. The site is a secluded place, as access to the rooftop is restricted, and the location and height of the building ensure a clear view with no obstruction by trees, vegetation or other buildings, reducing distorting effects. Still the measuring site is far from the standard installation at 2 m or 3 m above a flat surface, precluding standardisation (Harrison and Nicoll, 2018). Although the location is not ideal, particularly for electric field measurements – since the building and site conducting structures distort the local field – the effect is expected to be constant in time, as it is only a function of the non-varying site geometry, and rooftop measurements can be assumed to represent the local urban area (Matthews et al., 2019).

2.2. Instruments

The instruments measuring atmospheric electric field, gamma radiation, and radon concentration were each installed about 0.5 m apart (Fig. 2).

The vertical electric field is measured every 1-second with a Campbell CS 110 Electric Field Meter sensor recording the corresponding average value every 1-minute. Because of the complex site geometry, and since the main interest is on the relative variability rather than the absolute value of the atmospheric electric field, no specific site corrections are applied to the electric field measurements. A negative reading corresponds to a field vector pointing downward, driving a positive charge downwards. Here all the electric field measurements are displayed with the opposite sign, following the practice in atmospheric electricity (positive values under fair weather conditions).

Gamma radiation is measured with a 3"x 3" NaI(Tl) scintillator (Scionix, the Netherlands) equipped with an electronic total count Single Channel Analyzer (SCA) detecting gamma radiation in the energy range from 475 keV to 3 MeV. This arrangement allows to reduce the Compton background in the 50–475 keV low-energy range, improving the sensitivity of measurements (Zafrir et al., 2011). The sensor is encapsulated in a PVC casing for protection from environmental harsh conditions (particularly rain and humidity). Gamma radiation measurements are performed for sampling time intervals of 5 min.

Radon concentration is measured with a solid state silicon diode detector (Barasol BT45N, Algade Inc., France) detecting alpha particles between 1.5 MeV and 6 MeV. This sensor is particularly well suited for continuous measuring of radon concentration in soil and other high-radon environments, but clearly inadequate for atmospheric measurements due to its low sensitivity of typically 1 pulse per hour per 50 Bq/m3. Still integrated measurements over sampling times of 6 h are used for a qualitative indication of radon concentration in the air, despite the obvious limitation of the sensor.

The rooftop measurements are complemented by ERA5 hourly reanalysis surface data (Hersbach et al., 2018) from the model gridpoint closest to the measurement site (41.18 °N, 351.4 °E) and local meteorological information from ISEP station (≤ 1 km from the site) every 5-minutes. All times are in UT (Universal Time), and local time is WEST (West European Summer Time), UT+1.

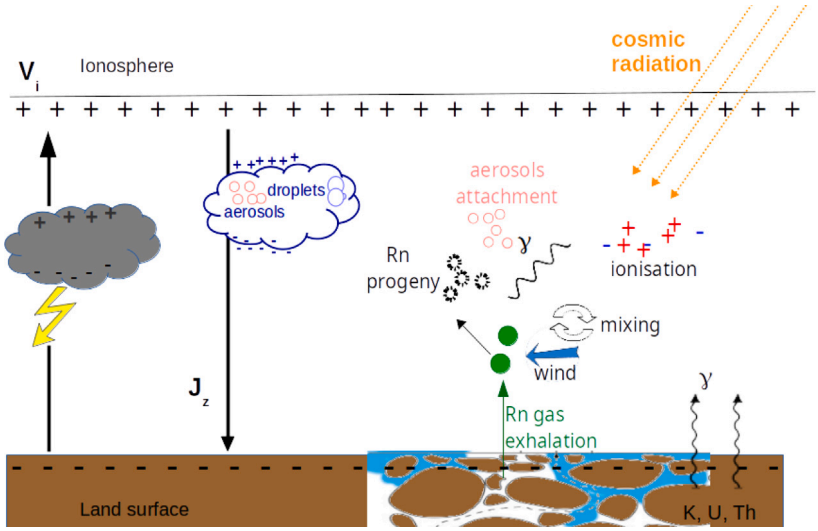

Fig. 1. Scheme of space–atmosphere–land interactions influencing ambient radioactivity and atmospheric electricity. Charge separation in each of the ~ 1000 thunderstorms active at any one time on Earth create a permanent potential difference between the ionosphere and the Earth's surface ($V_i \sim 250$ kV), which drives a vertical conduction current density ($J_z \sim 2pA/m^2$). The electrical conductivity of the atmosphere is due to the presence of ions arising from natural ionisation driven by ambient radioactivity (cosmic radiation, radon, and terrestrial gamma radiation).

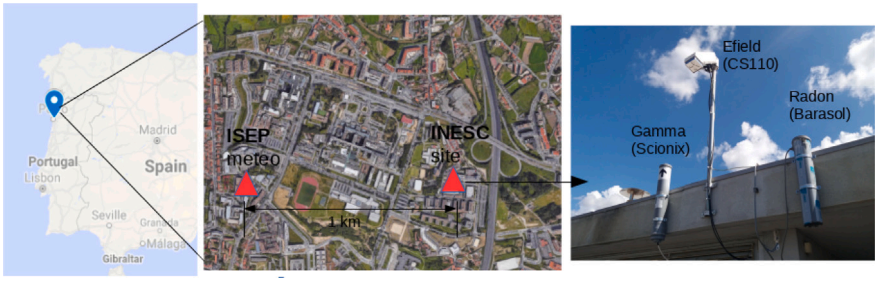

Fig. 2. Geographical setting: location map (left), location of the site and local meteorological station (middle) and measurement site (right).

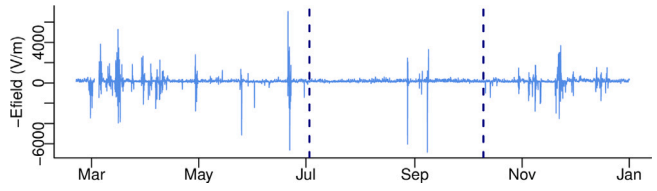

Fig. 3. Time series of hourly averaged electric field measurements from March to December 2018. The vertical lines indicate the period under analysis.

2.3. Data

The hourly time series of vertical electric field measurements collected from March to December 2018 is shown in Fig. 3. The atmospheric electric field displays very large variations, particularly in winter, when occurrences of disturbed weather are more frequent. In order to focus on the electric field variability under non-disturbed weather conditions, a subset of 100 days, from July to early October 2018, is considered hereafter (marked by vertical lines in Fig. 3). The few days in this period associated with disturbed weather (27 and 28 August, and from 3rd to 8th September), are discarded. The corresponding time series of hourly atmospheric electric field values is displayed in Fig. 4(a).

Fig. 4(b) shows the hourly time series of total gamma radiation counts for the same 100-days period. Gaps visible in the gamma time series are due to power supply shortages and resulting lack of measurements from the gamma scintillator. The time series of gamma counts displays well defined daily peaks, particularly in early August and mid-September.

Despite the already mentioned limitations of radon gas concentration measurements, the time series of radon concentration values is displayed in Fig. 4(c). In addition to the temporal sparsity resulting from the long 6-hour integration period, many values are missing as a result of below detection limit measurements.

All the results presented hereafter are based on the hourly-averaged time series (and 6-hour series in the case of radon), without any further pre-treatment — in particular missing values are kept unchanged, i.e. not interpolated.

2.4. Empirical Orthogonal Function (EOF) analysis

An Empirical Orthogonal Function (EOF) analysis of a 2-D dataset, also called principal component analysis (PCA) (Jollife, 2002) consists of an eigenanalysis of the data covariance matrix representing a coordinate transformation into new directions along which the maximum possible variance can be explained and in which the covariance matrix is diagonal (and thus the variations are uncorrelated with each other). This allows to represent the variability of a dataset in terms of a few patterns (designated by principal components) which are linear combinations of the original data explaining the maximum possible variance. The coefficients of the linear combination are the eigenvectors of the data covariance matrix.

In order to focus on the diurnal pattern, the hourly values of the time series are first organised as sub-series for each individual day into a $n \times m$ data matrix where $n = 24$ is the number of hours in a day

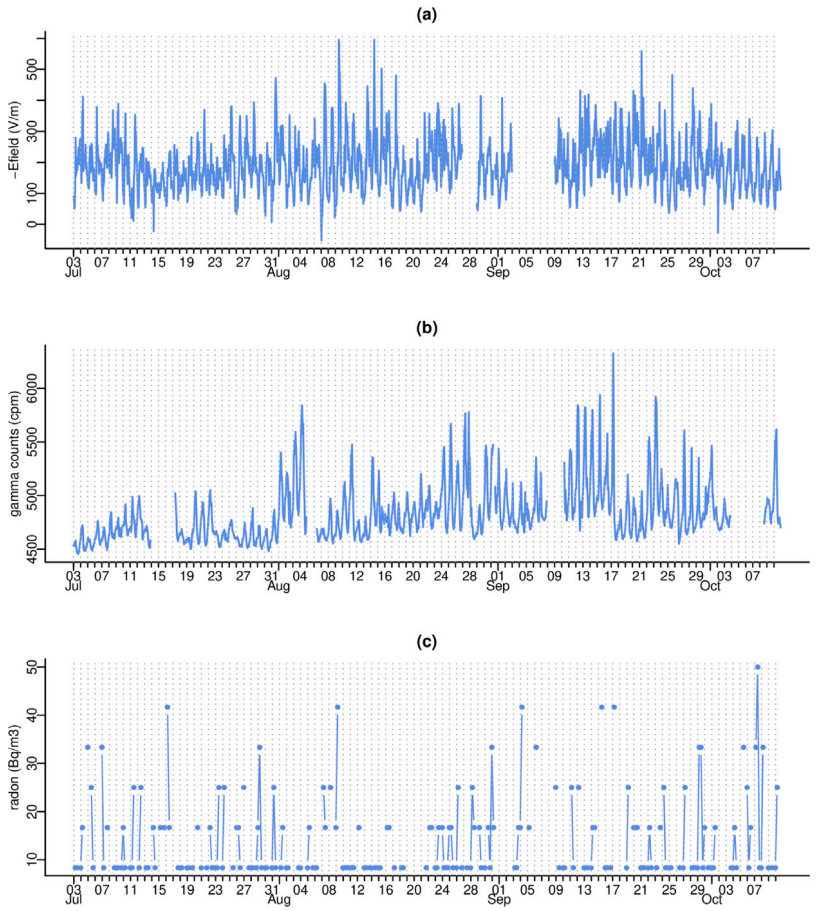

Fig. 4. Time series of (a) hourly averaged electric field measurements (July–October 2018), (b) hourly averaged total gamma radiation measurements, in counts per minute (cpm), and (c) radon gas concentration over 6-hour integration periods.

and m is the number of individual days. Although the total number of days in the time series under consideration is 100, days for which all the observations are missing are not included in the data matrix used for the EOF analysis. Furthermore, in order to take account of missing values in some hours of each day, the iterative procedure dineof (Data Interpolating Empirical Orthogonal Functions) described by Beckers and Rixen (2003) is used. The eigenanalysis of the data covariance matrix yields n eigenvectors (of size m) and n eigenvalues (which indicate how much variance is explained by each eigenvector). This allows to represent most of the variability in the original data by few ($< n$) modes of variability, each expressed by a principal component (linear combination of the data) and the corresponding eigenvector (the coefficients of the linear combination).

3. Results

3.1. Electric field

The temporal structure of the atmospheric electric field measurements is dominated by daily variability, as demonstrated by the cumulative spectrum of the electric field data in Fig. 5(a). The cumulative spectrum (Venables and Ripley, 2002) has the advantage of simplifying the visual inspection of the dominant periodicities in a time series and also of enabling the comparison of different time series (Barbosa et al., 2006).

The diurnal composite electric field for the whole 100-day period, summarised as a box-and-whisker plot (Fig. 5(b)) also shows a daily variation with higher values occurring around mid-day, and a secondary peak in the early morning between 6 and 8 UT. Fig. 5(b) also displays broad distributions for each hour of the day, reflecting large day to day variability, particularly during morning time.

Since the daily variation is the main feature in the atmospheric electric field time series, an EOF analysis is performed for a detailed description of the daily signal. The EOF analysis results indicate that almost 80% of the variability of the atmospheric electric field can be explained by only three modes of variability. The leading component, explaining more than 55% of the daily variability (Fig. 6(a)) corresponds to a daily cycle peaking in the early afternoon (14h-15h UT) and with minimum at 05h UT. The leading signal also exhibits a secondary peak around 08h UT following a sharp increase after sunrise. The second dominant mode of daily variability explains about 14% of the variance and reflects a pattern with lowest values in the evening (Fig. 6(b)). Finally the 3rd mode (Fig. 6(c)) accounts only for 8% of the variance, and corresponds to a daily pattern dominated by a sharp peak in the early morning (~8h00). The eigenvectors associated to these principal components (Fig. 7) can be interpreted as the weights of each component for each individual day. Fig. 7(a) confirms that the 1st mode is the typical daily pattern exhibited by the atmospheric electric field, with only a few days (25th July 25, 6th August and 1st October) with strongly deviating daily variation. In the case of the 2nd and 3rd modes the eigenvectors show a much more uneven temporal distribution, with both positive and negative values, indicating irregular weights for the corresponding maximum variance pattern (or the opposite pattern in case of negative values). The 2nd mode (Fig. 7(b)) identifies specific days for which the electric field is lowest in the evening (e.g. 25th July) as well as days for which the electric field peaks in the evening (e.g. 11th July). The 3rd mode (Fig. 7(c)) reflects early morning enhanced/decreased values of the atmospheric electric field and tends to be positive (reflecting early morning enhancement), except in the first half of August.

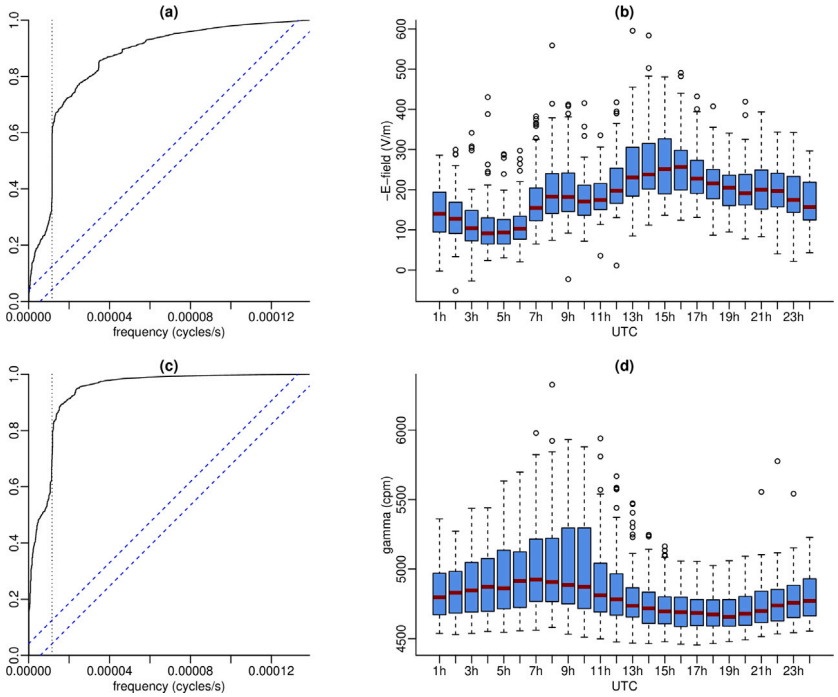

Fig. 5. Exploratory description of the hourly-averaged atmospheric electric field (top) and gamma radiation data (bottom). The left plots are cumulative spectra (the diagonal dashed lines represent the 95% confidence band of a white noise process, and the vertical dashed line the frequency of 1 cycle/day [1/(24×60×60)]). The right plots are composite plots summarising the values for each hour of the day (the low and high limits of the box are the 1st and 3rd quartiles of the data, respectively, with the horizontal line corresponding to the median value; the dashed lines extend from the limits of the box to 1.5 times the interquartile range, and values outside this interval are represented by open circles).

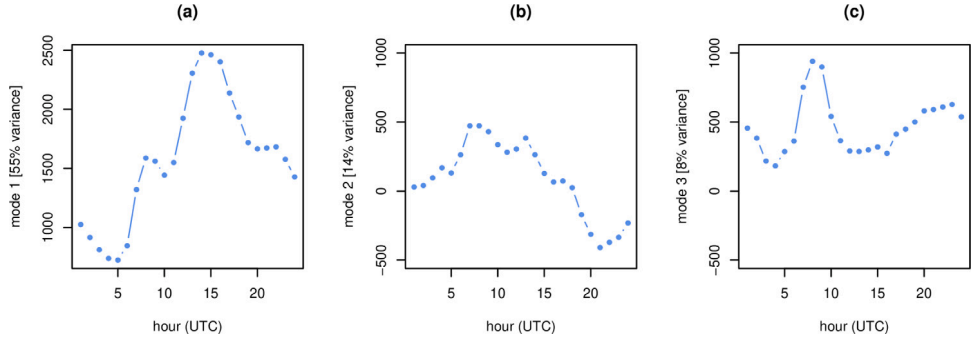

Fig. 6. Principal components reflecting the dominant patterns of daily variability of the atmospheric electric field: (a) mode 1; (b) mode 2; (c) mode 3.

3.2. Gamma radiation

As for the atmospheric electric field, the temporal structure of the gamma radiation measurements is dominated by daily variability, although the low-frequency variability is stronger in the gamma than in the electric field time series (Fig. 5(c)). On average higher gamma counts tend to occur in the early morning (~ 6h UT) and lowest gamma values in the mid-afternoon. The variance follows the mean, being smallest in the afternoon (Fig. 5(d)), a typical nonlinear feature of environmental radioactivity time series (Barbosa et al., 2007). The distribution of gamma counts in the early morning period (06-09 UT) is very asymmetric, reflecting the sharp peaks in gamma counts and the widespread range in maxima compared to relatively stabler baseline values. Outlying gamma counts larger than 6000 cpm in the early morning correspond to specific days with extreme high counts (4th August, 17th September).

A similar EOF analysis as for the electric field is performed for the daily sub-series of gamma radiation measurements. The daily pattern explaining the maximum fraction of the dataset variance (77%) is a cycle with a maximum around 08 UT and minimum at 19 UT (Fig. 8(a)). This is the most frequently occurring pattern (Fig. 9(a)), and only a few days (e.g 18th August, 2nd October) exhibit a clear distinct behaviour (none or very small daily variation). The 2nd mode (Figs. 8b and 9b) reflects days with a very early ~ 2*h* UT dominant peak and lowest values at mid-day (e.g. 1st September), as well as days with the opposite behaviour, low values in the early morning and peak at mid-day (e.g 15th September), corresponding to negative eiegenvectors values.

3.3. Radon

Despite the low quality of the radon concentration measurements, and the long integration time, a daily periodicity is still apparent in the average radon concentration, with lowest values in the afternoon period (12-18 UT) and highest before sunrise (00-06 UT), as shown in Fig. 10. This daily variability is consistent with the daily variation of gamma radiation, which includes the contribution of radon progeny.

Radon can be used as an indicator of atmospheric stability and mixing (Chambers et al., 2011; Williams et al., 2016). The radon measurements during the night (from 00h00 to 06h00), typically under stabler atmospheric conditions favouring radon accumulation near the

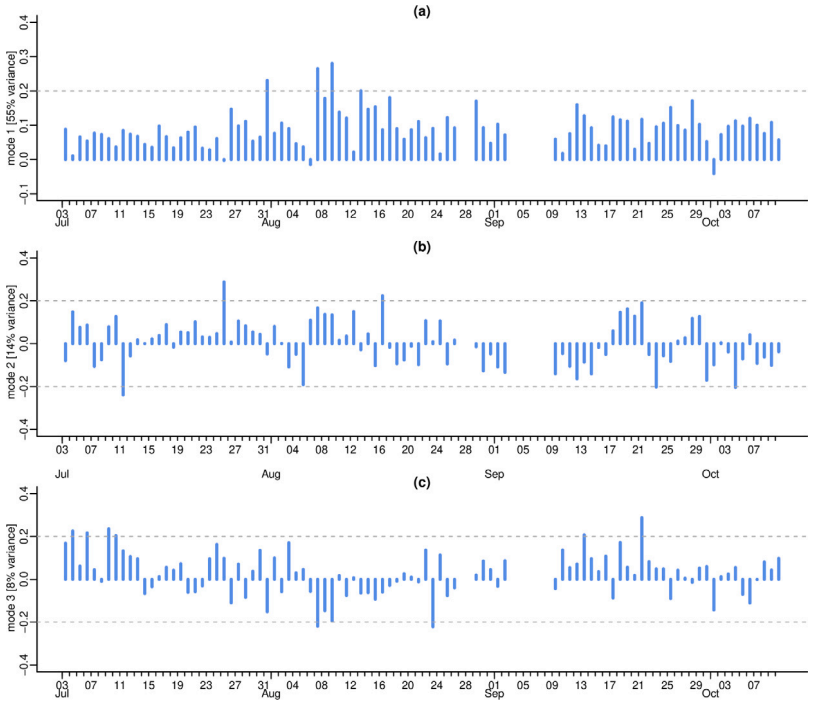

Fig. 7. Barplot of the eigenvectors associated to the patterns displayed in Fig. 6: (a) mode 1; (b) mode 2; (c) mode 3. Note: the horizontal dashed lines are visualisation aids only and do not represent statistical confidence limits.

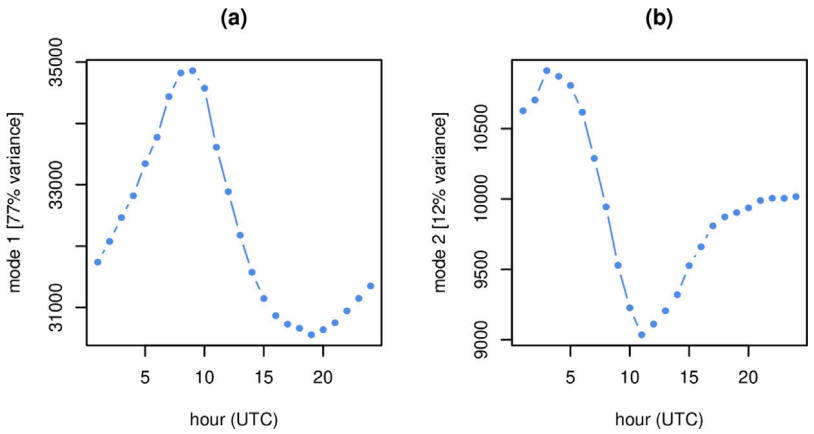

Fig. 8. Principal components reflecting the dominant patterns of daily variability of gamma radiation counts: (a) mode 1; (b) mode 2.

surface, are used to infer a radon-based mixing classification. Fig. 11(a) shows the histogram of the radon values for the 00-06 integration period, which displays 3 distinct groups: radon values below 10 Bq/m^3, between 15 and 25 Bq/m^3, and above 30 Bq/m^3. These intervals are considered for defining three classes of nocturnal radon concentration. Using a similar approach as in Chambers et al. (2019), one of these classes is then attributed to every value of the 6-hours time series of radon concentration based on the night value (00h-06h) over the 24-period covering a complete night from 18:00 to 12:00 the next day. Fig. 11(b) displays the resulting composite plot of radon concentration for each of the three classes.

4. Discussion

4.1. Atmospheric conditions

The summer/early autumn period considered in this study is characterised by variable atmospheric conditions, illustrated in Fig. 12 by the time series of local air temperature, relative humidity, wind speed and wind direction, and by the reanalysis time series of planetary boundary layer height. Temperatures were atypically low during the month of July (lowest average temperatures in the last 30 years) and humidity high, associated with the frequent occurrence of fog, particularly in the morning (IPMA, 2018). Conditions changed dramatically in August with the arrival of a very warm air mass from north Africa. The heat wave was accompanied by exceptionally high aerosol levels associated with the dust transported from Africa to Iberia, in particular coarse particles as indicated by AERONET (https://aeronet.gsfc.nasa.gov/) measurements (Giles et al., 2019) at Cabo da Roca (SW Portugal). The first days of August were exceptionally warm, 4th of August being classified as the hottest day of the 21st century in Portugal (IPMA, 2018). A further period of very high temperatures occurred from 18 to 21 August, although not associated to high levels of coarse aerosols as in early August. September was also a very warm and dry month with record-breaking temperatures in the first days of the month and further periods of very high temperature on 10–11th and 23–24th September. Early October was also exceptionally warm with maximum temperatures more than 9 °C above average values (IPMA, 2018).

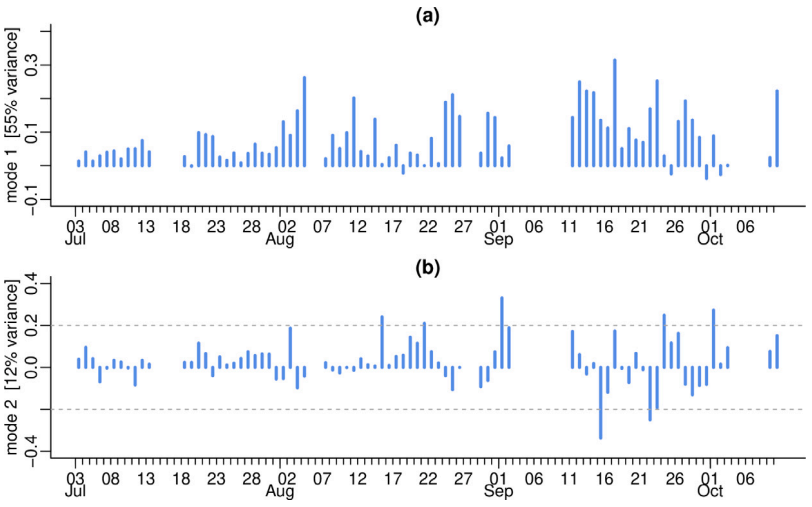

Fig. 9. Barplot of the eigenvectors associated to the patterns displayed in Fig. 8.

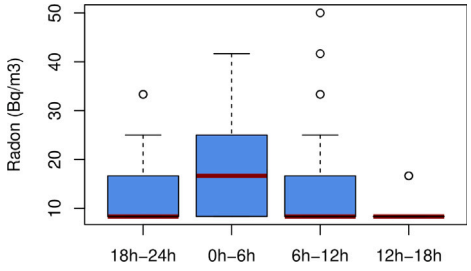

Fig. 10. Composite boxplots of radon concentration measurements (symbols as in Fig. 5(b)).

Table 1
Hourly correlation coefficients between gamma radiation and meteorological parameters (the sign * denotes correlations below 0.3).

	PBL height	Humidity	Temperature	Wind speed
Gamma (00-01 UT)	−0.59	−0.37	*	−0.37
Gamma (01-02 UT)	−0.55	−0.37	0.34	*
Gamma (02-03 UT)	−0.52	−0.33	0.31	−0.35
Gamma (03-04 UT)	−0.53	*	*	−0.31
Gamma (04-05 UT)	−0.55	*	*	−0.37
Gamma (05-06 UT)	−0.55	*	*	−0.36
Gamma (06-07 UT)	−0.56	*	*	−0.39
Gamma (07-08 UT)	−0.58	*	*	−0.43
Gamma (08-09 UT)	−0.70	*	*	−0.36
Gamma (09-10 UT)	−0.63	*	*	−0.38
Gamma (10-11 UT)	−0.41	*	*	−0.34
Gamma (11-12 UT)	*	*	0.38	−0.35
Gamma (12-13 UT)	*	*	0.35	*
Gamma (13-14 UT)	*	*	*	*
Gamma (14-15 UT)	*	*	0.34	*
Gamma (15-16 UT)	*	−0.33	0.41	*
Gamma (16-17 UT)	*	−0.44	0.47	*
Gamma (17-18 UT)	−0.33	−0.49	0.46	−0.33
Gamma (18-19 UT)	−0.52	−0.44	0.34	−0.32
Gamma (19-20 UT)	−0.68	−0.42	0.32	−0.52
Gamma (20-21 UT)	−0.57	−0.35	*	−0.56
Gamma (21-22 UT)	−0.49	−0.37	0.34	−0.47
Gamma (22-23 UT)	−0.50	−0.39	0.37	−0.43
Gamma (23-00 UT)	−0.56	−0.42	0.37	−0.45

4.2. Ambient radioactivity

Gamma radiation measurements include gamma rays from the interaction of secondary cosmic radiation with the atmosphere, gamma rays from terrestrial radionuclides (K, U, Th) and gamma rays from radon progeny. The cosmic contribution is modulated by solar variability and can be considered approximately constant over such a short period of a few months and for a constant altitude. The terrestrial contribution changes relatively slowly as it depends mostly on surface conditions affecting the subsurface propagation of gamma rays, particularly soil water content, (Barbosa et al., 2018). The radon progeny contribution is much more variable as it is very much affected by atmospheric conditions influencing the accumulation of radon gas near the ground, its mixing, and atmospheric transport. Thus the gamma measurements base level of ~ 4800 cpm (Fig. 4(b)) reflects mainly the cosmic contribution and the terrestrial background and is much stabler than the gamma variations related to radon and airborne radon progeny contributions that can reach more than 2000 cpm in a single day.

The daily variability of gamma radiation, typically peaking before sunrise and with a minimum in the afternoon, mainly reflects the radon

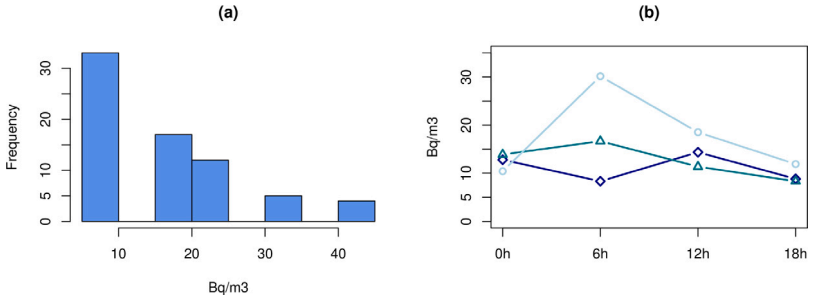

Fig. 11. (a) Histogram of radon concentration values in the period (00-06 UT); (b) average radon concentration for each of the radon-based stability classes: ◊ class 1 (< 10 Bq/m^3), ▵ class 2 (10–30 Bq/m^3) and ∘ class 3 (≥ 30 Bq/m^3).

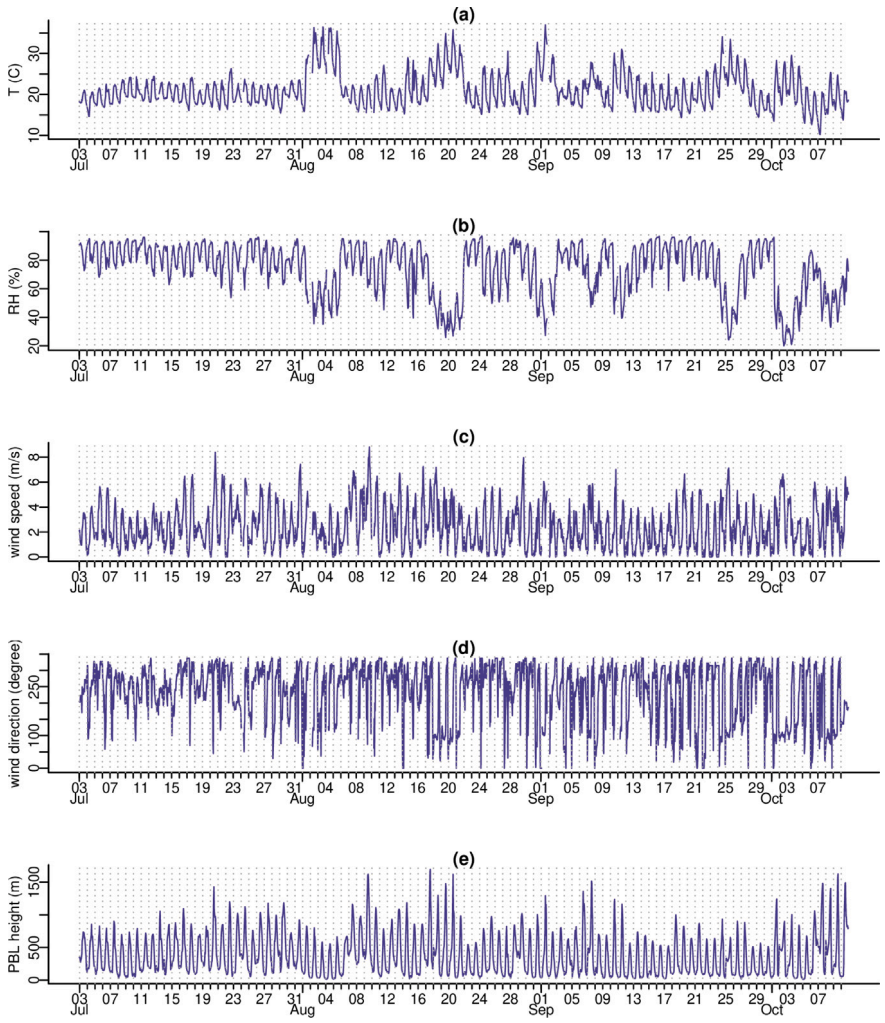

Fig. 12. Time series of local meteorological parameters: (a) air temperature, (b) relative humidity, (c) wind speed, (d) wind direction and (e) planetary boundary layer height from ERA5 reanalysis.

gas accumulation during the night, and therefore is strongly related to planetary boundary layer dynamics, decreasing with increasing mixing height and (to a lesser extent) with wind speed (Table 1). A few cases of approximately constant gamma radiation during the day, with no cyclic pattern (e.g. 18th August, 2nd October) are associated with conditions of high early morning temperature and low humidity (Fig. 12), which promote atmospheric mixing rather than the nocturnal accumulation of radon gas. The radon-based stability classification indicates that these days belong to class 1, characterised by very low radon concentration amplitude suggestive of windy and well-mixed conditions.

The daily range of gamma radiation variations is smaller in July (Fig. 4(b)), consistent with lower daily amplitudes in air temperature during July (Fig. 12(a)). Gamma radiation values are moderately associated with temperature in the afternoon (Table 1), when radon concentration is the lowest, likely as a result of the combined effect of increased radon exhalation (Lebedyte et al., 2003) and increased propagation range of terrestrial gamma radiation in drier soil. Although the heat wave period in the beginning of August coincides with a clear enhancement in gamma radiation, similar periods of very high temperatures (18th–21st August, 1st–2nd, 10th–11th and 23rd–24th September) are not associated with high gamma values (Figs. 4(b) and 12). This fact suggests that the enhancement in ambient radiation that occurred in early August is not driven only by temperature. The main difference between the early August heat wave and similar later periods of very high temperatures is the North Africa origin of the associated air mass and its high content of dust. The enhanced aerosol loading can explain the gamma radiation enhancement as the increase in coarse aerosols results in increased attached radon progeny, similarly to previous results showing gamma radiation enhancement driven by aerosols (Barbosa et al., 2017). The largest peak in gamma radiation on September 17th is also associated with enhanced aerosol loading (confirmed by AERONET measurements) rather than temperature.

A small negative correlation is identified for gamma radiation and air humidity for the period of lowest values of gamma radiation, in the evening and night (Table 1), along with a moderate positive correlation with temperature for the same period. Higher temperatures increase radon exhalation (and thus the airborne contribution to gamma radiation) while the corresponding drier environment decreases the attenuation of the surface contribution to gamma radiation.

4.3. Atmospheric electric field

The daily variability of the atmospheric electric field evident in the median hourly values (Fig. 5(b)) and summarised by the 1st EOF mode (Fig. 6(a)), exhibits a minimum at 03-05 UT and maximum at 13-15 UT, with decreasing values from ~ 22 UT up to 03-05 UT the next day. This diurnal variation seems dominated by local effects, as the expected maximum around 19 UT from the global atmospheric electric field contribution (peak of lightning activity over the Americas) is replaced by a clear early afternoon maximum around 15:00 UT. This deviation from the conventional Carnegie curve from marine measurements is hardly surprising given the land and even urban location of the site. At

Table 2
Correlation coefficients between eigenvectors of the atmospheric electric field and daily averaged meteorological parameters (the sign * denotes correlations below 0.3).

	Mode 1	Mode 2	Mode 3
Temperature	*	−0.33	*
Humidity	*	0.42	*
Wind speed	0.52	*	−0.39
PBL height	*	*	*

Table 3
Hourly correlation coefficients between electric field and environmental parameters (the sign * denotes correlations below 0.3).

	Gamma	PBL height	Humidity	Temperature	Wind speed
E (00-01 UT)	*	−0.42	0.3	*	−0.53
E (01-02 UT)	*	−0.40	0.32	*	−0.51
E (02-03 UT)	*	−0.40	0.46	−0.31	−0.53
E (03-04 UT)	*	−0.31	0.38	*	−0.35
E (04-05 UT)	*	*	0.43	−0.36	−0.33
E (05-06 UT)	*	*	0.45	*	−0.33
E (06-07 UT)	*	*	0.41	*	−0.31
E (07-08 UT)	*	*	0.50	−0.32	−0.43
E (08-09 UT)	*	*	0.47	*	−0.39
E (09-10 UT)	*	*	0.39	*	*
E (10-11 UT)	*	*	0.39	*	*
E (11-12 UT)	*	*	*	*	*
E (12-13 UT)	*	*	*	*	*
E (13-14 UT)	*	*	*	*	*
E (14-15 UT)	*	*	*	*	*
E (15-16 UT)	*	*	*	*	*
E (16-17 UT)	*	*	*	*	*
E (17-18 UT)	*	*	*	*	*
E (18-19 UT)	*	*	*	*	*
E (19-20 UT)	0.45	−0.47	*	*	−0.53
E (20-21 UT)	0.55	−0.53	*	*	−0.60
E (21-22 UT)	0.48	−0.47	*	*	−0.54
E (22-23 UT)	0.38	−0.47	*	*	−0.49
E (23-00 UT)	*	−0.40	*	*	−0.56

non-marine sites the atmospheric electric field often displays a diurnal pattern distinct from the Carnegie curve as a result of local effects associated with aerosol loading and ambient radioactivity (Harrison and Aplin, 2002; Kastelis and Kourtidis, 2016; Yaniv et al., 2016, 2017).

The atmospheric electric field at this urban site is typically lowest at dawn and maximum in the early afternoon. The dawn minimum is consistent with historical measurements of the atmospheric electric field in Porto (Serra do Pilar) but the historical measurements display a maxima in the evening rather than in the afternoon (Märcz and Harrison, 2005). Given the urban nature of the site, the atmospheric electric field enhancement currently observed in the early afternoon likely reflects aerosol effects. An increase in atmospheric pollution and aerosol loading is expected in the city of Porto relative to mid-20th century conditions.

The pattern of lowest electric field at dawn and highest in the early afternoon explains more than 50% of the daily variability in the local electric field (1st mode). Only a few cases of opposite daily variation (higher atmospheric electric field in the morning than in the evening) are pinpointed by the eigenvectors of the dominant mode (1st October, 6th August — see Fig. 7(a)). These are transition days associated with abrupt changes in atmospheric conditions: the end of the early August heat wave and associated abrupt increase in relative humidity on 6th August, and the onset of the early October heat wave and abrupt decrease in relative humidity on 1st October (see Fig. 12).

The daily time series of eigenvectors of the 1st mode (Fig. 7(a)), reflecting the relative importance of the mode 1 daily pattern (Fig. 6(a)), is correlated with daily averaged wind speed (Table 2). The days for which the mode 1 pattern is more evident, e.g. 31st July, 7th and 9th August (Fig. 7) are associated with strong winds (> 6 m/s) blowing from the North. The fact that the pattern is correlated with wind speed but not with the boundary layer height (Table 2) suggests that the dominant process is not vertical mixing and increased mixing layer height but local (horizontal) transport. Thus it is plausible that the afternoon increase of the electric field relative to the morning values (the dominant feature in the mode 1 pattern) is driven by an increase in aerosols transported from the northern industrial area. Aerosols reduce the amount of small ions through their attachment to aerosols, thus reducing atmospheric conductivity.

For the night and early morning periods the hourly electric field values tend to be anti-correlated with wind speed, as well as with the boundary layer height (Table 3). Conditions of low wind and shallow mixing height favour the accumulation of radon and radon progeny near the surface, increasing ion formation and thus increasing conductivity/decreasing the atmospheric electric field. However the fact that stable nocturnal boundary layer conditions are positively correlated with the atmospheric electric field indicates that ionising radiation is not the main factor influencing the atmospheric electric field in the night and early morning. A plausible alternative is the accumulation of aerosols in the stable nocturnal boundary layer, decreasing ion mobility and thus decreasing conductivity/increasing the atmospheric electric field.

The cases of days with lowest electric field in the evening rather than in the morning are not captured by mode 1 but by the 2nd mode (Fig. 6(b)). The associated temporal pattern is closely related to relative humidity, with positive eigenvectors, reflecting higher electric field in the morning than in the evening, associated with higher values of relative humidity (see Figs. 7b and 12b, and Table 2). Days dominated by this mode of variability, with high electric field in the morning rather than at mid-day and lowest in the evening (e.g. 25th July), are associated with occurrence of fog in the morning which enhances the electric field to values comparable to typical mid-day values. Fog increases the atmospheric electric field due to the attachment of small ions to water drops reducing the atmospheric conductivity (Bennett and Harrison, 2007). The daily pattern of lowest electric field in the evening described by the 2nd mode is also correlated with daily averaged temperature (Table 2) but this is very likely an indirect association resulting from the fact that relative humidity is anti-correlated with temperature (typically higher temperature is linked to drier conditions), also as no significant effect of temperature is detected in the hourly correlation values (Table 3).

In some days the atmospheric electric field shows similar values in the morning and evening, but a sharp peak in the early morning, from ~ 6 to 8 UT. This pattern of variation is captured by the 3rd EOF mode, but its relative importance is small, as it only explains less than 10% of the variability of the atmospheric electric field. The eigenvectors associated to this mode are typically positive, reflecting sunrise enhancement, except for periods (e.g. mid-August) of deep nocturnal boundary layer (see Figs. 7c and 12d). Table 2 shows a negative correlation for this mode, indicating that the occurrence of this pattern of early morning enhancement of the atmospheric electric field is associated with conditions of low wind.

In the evening (from ~ 19 to 23 UT) the atmospheric electric field is correlated with gamma radiation (Table 3) and anti-correlated with wind speed and the height of the planetary boundary layer. Shrinking of the planetary boundary after sunset tends to concentrate aerosols near the surface. Aerosols reduce conductivity due to the reduction of small ions via charge transfer and ion–aerosol attachment. Shallow mixing and low wind conditions also favour the accumulation of radon and its progeny, and the consequent increase in ionising radiation promotes ion formation and increased atmospheric conductivity. Thus in conditions of low wind speed and shallow mixing height both aerosols and gamma radiation influence the atmospheric electric field, with opposing effects. In the evening period gamma radiation is typically very low. The positive correlation between gamma radiation and the electric field suggests that aerosol-driven reduction in conductivity is the dominant influencing factor.

5. Conclusions

Ambient radioactivity is expected to influence the variability of the local atmospheric electric field, as natural ionising radiation is the main source of production of primary ions at the land surface, and ions play a key role in the electrical properties of the atmosphere. The electrical conductivity of the atmosphere depends on the ion concentration and size distribution, and thus on the balance between ion production, driven by ionising radiation, and loss to aerosols, via charge transfer and ion–aerosol attachment (Harrison and Carslaw, 2003; Harrison and Tammet, 2008; Harrison et al., 2010; Chen et al., 2016a).

Although ambient radioactivity and atmospheric conductivity are inter-related phenomena, the association between atmospheric electric field and natural radioactivity is not straightforward, as the variability of each parameter is *per se* strongly influenced by meteorological effects, particularly parameters associated with atmospheric stability, wind speed and boundary layer height. The present study shows, based on simultaneous measurements of electric field and natural radioactivity, that the variability of the local atmospheric electric field at such an urban environment is not dominated by ambient radioactivity but instead by local effects, particularly aerosol transport and accumulation close to the surface driven by local meteorological conditions. The results emphasise the complex interplay of atmospheric and surface conditions and that further investigation is required to better constrain and quantify the link between atmospheric electricity and ambient radioactivity.

Although an EOF analysis as the one presented here is only able to extract statistical modes, rather than physical modes, the decomposition of the atmospheric electric field performed in this study allowed to extract dominant patterns of variability, and to assess its association to local meteorological factors. EOF analysis is often used in climate studies, particularly for the identification of teleconnection patterns from space–time data, but rarely used in time series studies of ambient radioactivity or atmospheric electricity. As shown in the present study, the method can be applied for the identification of daily patterns in a flexible and robust way. Such patterns can be then further studied in detail, and even used as input to further methods e.g. machine learning approaches for pattern classification. Furthermore, EOF-derived dominant modes of variability can be useful for simplifying the comparison among different stations.

As the local atmospheric electric field is strongly influenced by atmospheric stability and mixing height, and radon is a very useful indicator of atmospheric stability (Chambers et al., 2019), a promising strategy, provided that instruments able to measure continuously the low concentration of radon in the atmosphere are available, is to use radon-based classification of atmospheric stability in atmospheric electricity studies.

Declaration of competing interest

The authors declare that they have no known competing financial interests or personal relationships that could have appeared to influence the work reported in this paper.

Acknowledgements

The invaluable technical assistance of Mr Manuel Domingos Silva from INESC TEC is gratefully acknowledged, as well as the assistance of Mr Alexandre Costa on data collection. Meteorological data from the ISEP station at the School of Engineering of the Polytechnic Institute of Porto (IPP) were kindly provided by José Oliveira. Thanks to Ana Maria Silva and Maria João Costa for their effort in establishing and maintaining the Cabo da Roca AERONET site. The contribution of fruitful discussions in the framework of COST Action Electronet (CA15211) is further acknowledged. This work is partially supported by Project "Coral - Sustainable Ocean Exploitation: Tools and Sensors/NORTE-01-0145-FEDER-000036", financed by the North Portugal Regional Operational Programme (NORTE 2020) under the PORTUGAL 2020 Partnership Agreement and by the European Regional Development Fund (ERDF). Support from National Funds through the Portuguese funding agency, FCT – Fundação para a Ciência e a Tecnologia within project UID/EEA/50014/2019 is also acknowledged.

References

Anisimov, S.V., Galichenko, S.V., Aphinogenov, K.V., Prokhorchuk, A.A., 2018. Evaluation of the atmospheric boundary-layer electrical variability. Bound.-Lay. Meteorol. 1–22.

Anisimov, S.V., Mareev, E.A., 2008. Geophysical studies of the global electric circuit. Izvestiya, Phys. Solid Earth 44 (10), 760.

Aplin, K.L., 2012. Smoke emissions from industrial western Scotland in 1859 inferred from Lord Kelvin's atmospheric electricity measurements. Atmos. Environ. 50, 373–376.

Aplin, K.L., Harrison, R.G., Rycroft, M.J., 2008. Investigating earth's atmospheric electricity: a role model for planetary studies. In: Planetary Atmospheric Electricity. Springer, pp. 11–27.

Arrillaga, J.A., de Arellano, J., Bosveld, F., Baltink, H.K., Yague, C., Sastre, M., Román-Cascon, C., 2018. Impacts of afternoon and evening sea-breeze fronts on local turbulence, and on CO2 and radon-222 transport. Q. J. R. Meteorol. Soc. 144 (713), 990–1011.

Barbosa, S.M., Donner, R.V., Steinitz, G., 2015. Radon applications in geosciences - progress & perspectives. Eur. Phys. J. Spec. Top. 224 (4), 597–603.

Barbosa, S., Huisman, J.A., Azevedo, E.B., 2018. Meteorological and soil surface effects in gamma radiation time series - implications for assessment of earthquake precursors. J. Environ. Radioact. 195, 72–78.

Barbosa, S.M., Miranda, P., Azevedo, E.B., 2017. Short-term variability of gamma radiation at the ARM Eastern North Atlantic facility (Azores). J. Environ. Radioact. 172, 218–231.

Barbosa, S.M., Silva, M.E., Fernandes, M.J., 2006. Wavelet analysis of the Lisbon and Gibraltar North Atlantic Oscillation winter indices. Int. J. Climatol. 26, 581–593.

Barbosa, S.M., Steinitz, G., Piatibratova, O., Silva, M.E., Lago, P., 2007. Radon variability at the Elat granite, Israel: Heteroscedasticity and nonlinearity. Geophysical Research Letters 34, L15309.

Barbosa, S.M., Zafrir, H., Malik, U., Piatibratova, O., 2010. Multiyear to daily radon variability from continuous monitoring at the Amram tunnel, southern Israel. Geophys. J. Int. 182, 829–842.

Beckers, J.M., Rixen, M., 2003. EOF Calculations and data filling from incomplete oceanographic datasets. J. Atmos. Ocean. Technol. 20 (12), 1839–1856.

Bennett, A.J., Harrison, R.G., 2007. Atmospheric electricity in different weather conditions. Weather 62 (10), 277–283.

Bossew, P., Cinelli, G., Hernández-Ceballos, M., Cernohlawek, N., Gruber, V., Dehandschutter, B., Menneson, F., Bleher, M., Stohlker, U., Hellmann, I., Weiler, F., Tollefsen, T., Tognoli, P., de Cort, M., 2017. Estimating the terrestrial gamma dose rate by decomposition of the ambient dose equivalent rate. J. Environ. Radioact. 166, 296–308.

Chambers, S.D., Podstawczynska, A., Pawlak, W., Fortuniak, K., Williams, A.G., Griffiths, A.D., 2019. Characterizing the state of the urban surface layer using radon-222. J. Geophys. Res.: Atmos. 124.

Chambers, S., Williams, A., Zahorowski, W., Griffiths, A., Crawford, J., 2011. Separating remote fetch and local mixing influences on vertical radon measurements in the lower atmosphere. Tellus B 63 (5), 843–859.

Chen, X., Kerminen, V.-M., Paatero, J., Paasonen, P., Manninen, H.E., Nieminen, T., Petäjä, T., Kulmala, M., 2016a. How do air ions reflect variations in ionising radiation in the lower atmosphere in a boreal forest?. Atmos. Chem. Phys. 16 (22), 14297–14315.

Chen, X., Paatero, J., Kerminen, V.M., Riuttanen, L., Hatakka, J., Hiltunen, V., Paasonen, P., et al., 2016b. Responses of the atmospheric concentration of radon-222 to the vertical mixing and spatial transportation. Boreal Enviro. Res. (21), 299–318.

Fricke, R.G.A., Schlegel, K., 2017. Julius Elster and Hans Geitel – Dioscuri of physics and pioneer investigators in atmospheric electricity. History Geo- Space Sci. 8 (1), 1–7.

Gasser, E., Nachab, A., Nourreddine, A., Roy, C., Sellam, A., 2014. Update of 40K and 226Ra and 232Th series gamma-to-dose conversion factors for soil. J. Environ. Radioact. 138, 68–71.

Giles, D.M., Sinyuk, A., Sorokin, M.G., Schafer, J.S., Smirnov, A., Slutsker, I., Eck, T.F., Holben, B.N., Lewis, J.R., Campbell, J.R., Welton, E.J., Korkin, S.V., Lyapustin, A.I., 2019. Advancements in the aerosol robotic network (AERONET) version 3 database – automated near-real-time quality control algorithm with improved cloud screening for sun photometer aerosol optical depth (AOD) measurements. Atmos. Meas. Tech. 12 (1), 169–209.

Goldhagen, P., 2000. Overview of aircraft radiation exposure and recent ER-2 measurements. Health Phys. 79 (5), 526–544.

Grundel, M., Porstendorfer, J., 2004. Differences between the activity size distributions of the different natural radionuclide aerosols in outdoor air. Atmos. Environ. 38 (22), 3723–3728.
Harrison, R.G., 2013. The Carnegie Curve. Surv. Geophys. 34 (2), 209–232.
Harrison, R., Aplin, K., 2002. Mid-nineteenth century smoke concentrations near London. Atmos. Environ. 36 (25), 4037–4043.
Harrison, R., Aplin, K., 2003. Nineteenth century Parisian smoke variations inferred from Eiffel Tower atmospheric electrical observations. Atmos. Environ. 37 (38), 5319–5324.
Harrison, R., Aplin, K., Rycroft, M., 2010. Atmospheric electricity coupling between earthquake regions and the ionosphere. J. Atmos. Sol.-Terr. Phys. 72 (5–6), 376–381.
Harrison, R.G., Carslaw, K.S., 2003. Ion-aerosol-cloud processes in the lower atmosphere. Rev. Geophys. 41 (3).
Harrison, R., Nicoll, K., 2018. Fair weather criteria for atmospheric electricity measurements. J. Atmos. Sol.-Terr. Phys. 179, 239–250.
Harrison, R.G., Nicoll, K.A., Aplin, K.L., 2017. Evaluating stratiform cloud base charge remotely. Geophys. Res. Lett. 44 (12), 6407–6412.
Harrison, R.G., Nicoll, K.A., Marlton, G.J., Ryder, C.L., Bennett, A.J., 2018. Saharan dust plume charging observed over the UK. Environ. Res. Lett. 13 (5), 054018.
Harrison, R.G., Tammet, H., 2008. Ions in the terrestrial atmosphere and other solar system atmospheres. Space Sci. Rev. 137 (1), 107–118.
Hersbach, H., de Rosnay, P., Bell, B., et al., 2018. Operational global reanalysis: progress, future directions and synergies with NWP. (27), URL https://www.ecmwf.int/node/18765.
Hess, V.F., 1912. Über Beobachtungen der durchdringenden Strahlung bei sieben Freiballonfahrten. Phys. Z. 13, 1084–1091.
IPMA, 2018. Boletim climatológico, ISSN 2183-1076. Technical Report, IPMA - Instituto Português do Mar e da Atmosfera.
Israelsson, S., Lelwala, R., 1999. Space charge density measurements downwind from a traffic route. Atmos. Res. 51 (3), 301–307.
Jollife, I., 2002. Principal Component Analysis 2 Edition Springer.
Kartalev, M., Rycroft, M., Fuellekrug, M., Papitashvili, V., Keremidarska, V., 2006. A possible explanation for the dominant effect of South American thunderstorms on the Carnegie curve. J. Atmos. Sol.-Terr. Phys. 68 (3), 457–468.
Kastelis, N., Kourtidis, K., 2016. Characteristics of the atmospheric electric field and correlation with CO2 at a rural site in southern Balkans. Earth Planets Space 68 (1), 1–15.
Latha, R., 2007. Micrometeorological influences and surface layer radon ion production: Consequences for the atmospheric electric field. Atmos. Environ. 41, 867–877.
Lebedyte, M., Butkus, D., Morkunas, G., 2003. Variations of the ambient dose equivalent rate in the ground level air. J. Environ. Radioact. 64 (1), 45–57.
Lopes, F., Silva, H.G., Bárias, S., Barbosa, S.M., 2015. Preliminary results on soil-emitted gamma radiation and its relation with the local atmospheric electric field at Amieira (Portugal). J. Phys. Conf. Ser. 646 (1), 012015.
Märcz, F., Harrison, R.G., 2005. Further signatures of long-term changes in atmospheric electrical parameters observed in Europe. Ann. Geophys. 23 (6), 1987–1995.
Matthews, J., Wright, M., Clarke, D., Morley, E., Silva, H., Bennett, A., Robert, D., Shallcross, D., 2019. Urban and rural measurements of atmospheric potential gradient. J. Electrost. 97, 42–50.
Melintescu, A., Chambers, S., Crawford, J., Williams, A., Zorila, B., Galeriu, D., 2018. Radon-222 related influence on ambient gamma dose. J. Environ. Radioact. 189, 67–78.
Nagaraja, K., Prasad, B.S.N., Srinivas, N., Madhava, M., 2006. Electrical conductivity near the Earth's surface: Ion-aerosol model. J. Atmos. Sol.-Terr. Phys. 68, 757–768.
Nicoll, K.A., Harrison, R.G., 2016. Stratiform cloud electrification: comparison of theory with multiple in-cloud measurements. Q. J. R. Meteorol. Soc. 142 (700), 2679–2691.
Paatero, J., Hatakka, J., 1999. Wet deposition efficiency of short-lived radon-222 progeny in central Finland. Boreal Env. Res. 4, 285–293.
Pal, S., Lopez, M., Schmidt, M., Ramonet, M., Gibert, F., Xueref-Remy, I., Ciais, P., 2015. Investigation of the atmospheric boundary layer depth variability and its impact on the 222-Rn concentration at a rural site in France. J. Geophys. Res.: Atmos. 120 (2), 623–643.
Piper, I.M., Bennett, A.J., 2012. Observations of the atmospheric electric field during two case studies of boundary layer processes. Environ. Res. Lett. 7 (1), 014017.
Porstendörfer, J., Zock, C., Reineking, A., 2000. Aerosol size distribution of the radon progeny in outdoor air. J. Environ. Radioact. 51, 37 – 48.
Price, C., 1993. Global surface temperatures and the atmospheric electrical circuit. Geophys. Res. Lett. 20, 1363–1366.
Rycroft, M.J., Harrison, R.G., 2012. Electromagnetic atmosphere-plasma coupling: The global atmospheric electric circuit. Space Sci. Rev. 168, 363–384.
Rycroft, M., Israelsson, S., Price, C., 2000. The global atmospheric electric circuit, solar activity and climate change. J. Atmos. Sol.-Terr. Phys. 62 (17), 1563–1576.
Sesana, L., Ottobrini, B., Polla, G., Facchini, U., 2006. 222-Rn as indicator of atmospheric turbulence: measurements at Lake Maggiore and on the pre-Alps. J. Environ. Radioact. 86 (2), 271–288.
Silva, H., Lopes, F., Pereira, S., Nicoll, K., Barbosa, S., Conceição, R., Neves, S., Harrison, R., Pereira, M.C., 2016. Saharan dust electrification perceived by a triangle of atmospheric electricity stations in Southern Portugal. J. Electrost. 84, 106–120.
Venables, W.N., Ripley, B.D., 2002. Modern Applied Statistics with S, third ed. Springer.
Wang, Y., Wang, Y., Duan, J., Cheng, T., Zhu, H., Xie, X., Liu, Y., Ling, Y., Li, X., Wang, H., et al., 2018. Temporal variation of atmospheric static electric field and air ions and their relationships to pollution in Shanghai. Aerosol Air Qual. Res. 18, 1631–1641.
Williams, E.R., 2009. The global electrical circuit: A review. Atmos. Res. 91 (2–4), 140–152.
Williams, A., Chambers, S., Conen, F., Reimann, S., Hill, M., Griffiths, A., Crawford, J., 2016. Radon as a tracer of atmospheric influences on traffic-related air. Tellus B 68, 30967.
Williams, A.G., Zahorowski, W., Chambers, S., Griffiths, A., Hacker, J.M., Element, A., Werczynski, S., 2011. The vertical distribution of radon in clear and cloudy daytime terrestrial boundary layers. J. Atmos. Sci. 68, 155–174.
Wilson, C.T.R., 1921. III. Investigations on lighting discharges and on the electric field of thunderstorms. Philos. Trans. R. Soc. Lond. Ser. A 221 (582–593), 73–115.
Wilson, C.T.R., 1924. The electric field of a thundercloud and some of its effects. Proc. Phys. Soc. London 37 (1), 32D–37D.
Wissmann, F., Dangendorf, V., Schrewe, U., 2005. Radiation exposure at ground level by secondary cosmic radiation. Radiat. Meas. 39 (1), 95–104.
Wright, M.D., Holden, N.K., Shallcross, D.E., Henshaw, D.L., 2014. Indoor and outdoor atmospheric ion mobility spectra, diurnal variation, and relationship with meteorological parameters. J. Geophys. Res.: Atmos. 119 (6), 3251–3267.
Yair, Y., Katz, S., Yaniv, R., Ziv, B., Price, C., 2016. An electrified dust storm over the Negev desert, Israel. Atmos. Res. 181, 63–71.
Yaniv, R., Reuveni, Y., Yair, Y., L., B., 2019. Temporal variations of the conduction current density during fair weather days in Israel. Atmos. Res. 222, 1–11.
Yaniv, R., Yair, Y., Price, C., Katz, S., 2016. Local and global impacts on the fair-weather electric field in Israel. Atmos. Res. 172, 119–125.
Yaniv, R., Yair, Y., Price, C., Mkrtchyan, H., Lynn, B., Reymers, A., 2017. Ground-based measurements of the vertical E-field in mountainous regions and the Austausch effect. Atmos. Res. 189, 127–133.
Zafrir, H., Barbosa, S.M., Malik, U., 2013. Differentiation between the effect of temperature and pressure on radon within the subsurface geological media. Radiat. Meas. 49, 39–56.
Zafrir, H., Haquin, G., Malik, U., Barbosa, S., Piatibratova, O., Steinitz, G., 2011. Gamma versus alpha sensors for Rn-222 long-term monitoring in geological environments. Radiat. Meas. 46 (6–7), 611–620.
Zhang, K., Feichter, J., Kazil, J., Wan, H., Zhuo, W., Griffiths, A.D., Sartorius, H., Zahorowski, W., Ramonet, M., Schmidt, M., Yver, C., Neubert, R.E.M., Brunke, E.-G., 2011. Radon activity in the lower troposphere and its impact on ionization rate: a global estimate using different radon emissions. Atmos. Chem. Phys. 11 (15), 7817–7838.